THE ROLE OF CLOUDS/RADIATION IN LONG-RANGE NUMERICAL WEATHER PREDICTION*

Zheng Qinglin (郑庆林)

Academy of Meteorological Science, State Meteorological Administration, Beijing

and *Kuo-Nan Liou*

University of Utah, Salt Lake City, Utah 84112, U.S.A.

Received February 23, 1989

ABSTRACT

We investigate the role of clouds and radiation in the general circulation of the atmosphere using a model designed for 30-day predictions. Comprehensive verifications of 30-day predictions for the 500 hPa geopotential height field have been carried out, using the data from ECMWF objective analyses that cover the period from May 5 to June 3, 1982. We perform three model simulations, including experiments with interactive cloud formation, without clouds, and without radiative heating. The latter two experiments allow us to study the effects of cloud/radiation interactions and feedbacks on the predicted vertical velocity, and the meridional and zonal wind profiles, averaged over a 30-day period.

We demonstrate that the Hadley circulation is maintained by the presence of clouds. The radiative cooling in the atmosphere intensifies the vertical motion in low latitudes and, to some extent, also strengthens the overall meridional circulation. The meridional winds are correctly reproduced in the model if clouds are incorporated.

The zonal winds are significantly affected by clouds and radiative cooling. Without an appropriate incorporation of these physical elements, the model results would deviate significantly from observations. The presence of clouds strengthens the westerlies in middle and high levels. In May, the northerly movement of the jet stream over eastern Asia is, in part, associated with the presence of clouds.

I. INTRODUCTION

Clouds are the primary modulators of the radiation balance of the earth-atmosphere system, as well as the heat transfer at the surface. Through condensation and precipitation, clouds also have a direct impact on the dynamic and hydrological processes in the atmosphere. Analyses of satellite-observed radiances have shown that the radiation budgets at the top of the atmosphere are largely controlled by the cloud field (e.g., Ramanathan, 1987). Certain clouds, such as stratus, are primarily responsible for the reflection of solar radiation, whereas others (cirrus) are important greenhouse modulators (e.g., Liou, 1986). Climate perturbation experiments have illustrated that a small change in cloudiness can significantly amplify or offset temperature increases due to external radiative forcing such as the anticipated increase in CO_2 (Wetherald and Manabe, 1988).

It is evident that cloud/radiation processes are important in the simulation of the earth's climate and climatic perturbations. However, the relevance of these processes to medium- and long-range weather prediction, and the extent and degree to which prediction experiments can be improved by a consistent integration of cloud and radiation processes in models

* This research wes supported by the Air Force Office of Scientific Grant AFOSR-87—0294.

are questions still open for scientific investigation and debate. In an attempt to understand the intricate interactions of radiation, clouds, and dynamic processes, Liou and Zheng (1984) performed numerical experiments using a GCM that was designed for short- and medium-range weather prediction. There are numerous findings regarding the quantitative effects of cloud/radiation interactions on temperature and cloud prediction in a 10-day prediction experiment. In particular, it has been demonstrated that radiative heating profiles in tropical regions are critical to the maintenance of the Hadley circulation.

In recent years, there have been significant advances in long-range numerical weather prediction. Miyakoda et al. (1983) successfully simulated the weather events of January 1977 and predicted a record-breaking cold spell over the eastern United States. Numerous studies (Smagorinsky, 1969; Gilchrist, 1977; Miyakoda et al., 1986) showed that time averaging over daily forecasts is useful in long-range weather prediction. This averaging can filter out small-scale and short-lived atmospheric perturbations and, at the same time, also reduce the influence of phase errors. Shukla (1981) performed a large number of experiments to test the predictability of long-range forecasts. He found that the predictability is about two weeks for synoptical scales and about four to six weeks for planetary scales. Predictability depends heavily on the initial conditions used in the experiment. Lorentz (1984) pointed out that the nonlinear terms imply the amplification of error. Errors in these terms must be reduced in order to perform long-range forecasts. Lorentz also stated that "... other candidates for incorporation or more refined formulation in future models appear to include various phenomena associated with water in the atmosphere, including clouds and precipitation, and the effects of these upon short-wave and long-wave radiation. These may be particularly important in establishing our ideas regarding the predictability of tropical weather."

It is the objective of this paper to investigate the role of clouds and coupled radiative effects on the general circulation of the atmosphere, using a GCM that is designed for 30-day predictions. The present model is based on the one described by Liou and Zheng (1984) and Zheng and Liou (1986), with specific modifications and refinements for long-range numerical weather prediction. In Section II, we briefly describe the manner in which the nonlinear and pressure gradient force terms in the σ-coordinate are computed. Verification of the model performance is given in Section III. In Section IV, we present the effects of clouds and radiative heating on the 30-day averaged vertical velocity, and meridional and zonal winds. Finally, conclusions are given in Section V.

II. THE MODEL

The present general circulation model, designed for long-range weather prediction, is a seven-level global spectral model based on the four-level and seven-level spectral models originally developed by Zheng (1979, 1981). Important modifications on the model physics, including radiative transfer, large-scale cloud formation, and cumulus convection, as well as the appropriate treatment of mountain effects, have been described in our recent papers (Liou and Zheng, 1984; Zheng and Liou, 1986). In this model, we have designed a specific numerical scheme to reduce computational errors in the nonlinear terms of the dynamic and thermodynamic equations. Below, we briefly describe the computational methodology, which is important in the performance of long-range prediction.

The governing equations for motion, temperature, and water vapor fields, as well as the continuity equation, the equation of state, and the equation for surface pressure are as follows:

$$\frac{\partial u}{\partial t}+fv=B_\lambda^\phi+E^u, \tag{1}$$

$$\frac{\partial v}{\partial t}-fu=B_\theta^\phi+E^v, \tag{2}$$

$$\frac{\partial T}{\partial t}-\hat{\lambda}\dot{\sigma}=E^T, \tag{3}$$

$$\frac{\partial q}{\partial t}=E^q, \tag{4}$$

$$\frac{1}{a\sin\theta}\left[\frac{\partial u}{\partial\lambda}+\frac{\partial}{\partial\theta}(v\sin\theta)\right]+\frac{\partial\dot{\sigma}}{\partial\sigma}=E^I-\hat{E}^I, \tag{5}$$

$$T=-\frac{\sigma}{R}\frac{\partial\phi}{\partial\sigma}, \tag{6}$$

$$\frac{\partial}{\partial t}\ln P_*=\hat{E}^I, \tag{7}$$

where

$$E^u=u\left[-\frac{1}{a\sin\theta}\frac{\partial u}{\partial\lambda}-\frac{v}{a}\mathrm{ctg}\theta\right]-\frac{v}{a}\frac{\partial u}{\partial\theta}-\dot{\sigma}\frac{\partial u}{\partial\sigma}+B_\lambda^T+F^u+\frac{g}{P_*}\frac{\partial\tau^u}{\partial\sigma}, \tag{8}$$

$$E^v=u\left[-\frac{1}{a\sin\theta}\frac{\partial v}{\partial\lambda}+\frac{u}{a}\mathrm{ctg}\theta\right]-\frac{v}{a}\frac{\partial v}{\partial\theta}-\dot{\sigma}\frac{\partial v}{\partial\sigma}+B_\theta^T+F^v+\frac{g}{P_*}\frac{\partial\tau^v}{\partial\sigma}, \tag{9}$$

$$E^T=-\frac{u}{a\sin\theta}\frac{\partial T}{\partial\lambda}-\frac{v}{a}\frac{\partial T}{\partial\theta}-\dot{\sigma}\frac{\partial\bar{T}}{\partial\sigma}+\frac{R\bar{T}}{C_p}\frac{\omega}{p}+\frac{R}{C_p}T_0\frac{d}{dt}\ln P_*+Q^L+Q^R+F^T+\frac{g}{P_*}\frac{\partial\tau^T}{\partial\sigma}, \tag{10}$$

$$E^q=-\frac{u}{a\sin\theta}\frac{\partial q}{\partial\lambda}-\frac{v}{a}\frac{\partial q}{\partial\theta}-\dot{\sigma}\frac{\partial q}{\partial\sigma}+q^L+F^q+\frac{g}{P_*}\frac{\partial\tau^q}{\partial\sigma}, \tag{11}$$

$$E^I=-\frac{u}{a\sin\theta}\frac{\partial}{\partial\lambda}\ln P_*-\frac{v}{a}\frac{\partial}{\partial\theta}\ln P_*, \tag{12}$$

$$\hat{E}^I=-\int_0^1\left\{\frac{1}{a\sin\theta}\left[\frac{\partial u}{\partial\lambda}+\frac{\partial}{\partial\theta}(v\sin\theta)\right]-E^I\right\}d\sigma, \tag{13}$$

$$\hat{\lambda}=\frac{R}{C_p}\frac{T_0}{\sigma}-\frac{\partial T_0}{\partial\sigma}. \tag{14}$$

In these equations, θ is the co-latitude, λ the longitude, a the radius of the earth, $\sigma=P/P_*$, P_* the surface pressure, R the gas constant for air, C_p the specific heat at constant pressure, $\omega/p=\dot{\sigma}/\sigma+\dot{P}_*/P_*$, $T=T_0+\bar{T}$, T_0 the horizontal averaged temperature at time t_0, $\bar{T}$ the temperature deviation from T_0, Q^L the sum of the heating rate due to large-scale condensation and cumulus convection, q^L the corresponding water vapor sink, Q^R the heating rate due to radiative transfer, F^A and $(g/P_*)\,\partial\tau^A/\partial\sigma$, the horizontal and vertical diffusion terms, respectively, where A denotes u, v, T, or q, and other notations are conventional.

The terms B^{ϕ} and B^{T}, defined in Eqs. (1), (2), (8) and (9), represent pressure gradient forces and are given by

$$B^{\phi}_{\lambda}=-\frac{1}{a\sin\theta}\frac{\partial\phi}{\partial\lambda}-\frac{R\bar{T}_0}{a\sin\theta}\frac{\partial}{\partial\lambda}\ln P_*, \tag{15a}$$

$$B^{\phi}_{\theta}=-\frac{1}{a}\frac{\partial\phi}{\partial\theta}-\frac{R\bar{T}_0}{a}\frac{\partial}{\partial\theta}\ln P_*, \tag{15b}$$

$$B^{T}_{\lambda}=\frac{R\bar{T}}{a\sin\theta}\frac{\partial}{\partial\lambda}\ln P_*, \tag{15c}$$

$$B^{T}_{\theta}=-\frac{R\bar{T}}{a}\frac{\partial}{\partial\theta}\ln P_*. \tag{15d}$$

The computation of pressure gradient force terms, using the σ-coordinate system in the vicinity of mountains, produces a problem that is associated with small differences between two large quantities. Below, we introduce an efficient scheme to remove this problem. Let ψ and χ denote the stream function and velocity potential, respectively. Equations (1), (2), and (5) may be expressed in terms of ψ and χ in the forms

$$\frac{\partial}{\partial t}\nabla^2\psi+f\nabla^2\chi=E^A+L^A, \tag{16}$$

$$\frac{\partial}{\partial t}\nabla^2\chi-f\nabla^2\chi+\nabla^2\phi+R\bar{T}_0\nabla^2\ln P_*=E^B+L^B, \tag{17}$$

$$\nabla^2\chi+\frac{\partial\dot{\sigma}}{\partial\sigma}=E^f-\hat{E}^f, \tag{18}$$

where

$$E^A=\frac{1}{a\sin\theta}\left[\frac{\partial}{\partial\theta}\sin\theta E^u-\frac{\partial}{\partial\lambda}E^v\right], \tag{19a}$$

$$E^B=\frac{1}{a\sin\theta}\left[\frac{\partial}{\partial\theta}\sin\theta E^v+\frac{\partial}{\partial\lambda}E^u\right], \tag{19b}$$

and L^A and L^B denote linear terms in the velocity and divergence equations defined in Zheng (1981). The velocity potential, χ, and vertical velocity, $\dot{\sigma}$, are related through Eqs. (17), (6) and (3) and can be expressed by

$$\begin{aligned}&\frac{\partial}{\partial\sigma}\frac{\partial^2}{\partial t^2}\nabla^2\chi-\frac{\hat{\lambda}R}{\sigma}\nabla^2\dot{\sigma}\\&=\frac{R}{\sigma}\nabla^2E^T+\frac{\partial}{\partial\sigma}\left[f\frac{\partial}{\partial t}\nabla^2\psi+\frac{\partial}{\partial t}(E^B+L^B)\right]-R\frac{\partial\bar{T}_0}{\partial\sigma}\nabla^2\hat{E}^f.\end{aligned} \tag{20}$$

Using the semi-implicit time integration scheme, Eqs. (20), (18) and (16) become

$$\begin{aligned}&-\lambda\nabla^2\dot{\sigma}^{t+\Delta t}-\frac{\partial^2}{\partial\sigma^2}\dot{\sigma}^{t+\Delta t}=\frac{\Delta t^2}{\sigma}R\nabla^2E^T\\&+\Delta t\frac{\partial}{\partial\sigma}\left[\frac{1}{2}\nabla^2f(\psi^{t+\Delta t}-\psi^{t-\Delta t})+E^B-E^{B,t-\Delta t}+\frac{1}{2}(L^{B,t+\Delta t}-L^{B,t-\Delta t})\right.\\&\left.+\frac{1}{\Delta t}\nabla^2(2\chi-\chi^{t-\Delta t})-\frac{1}{\Delta t}E^f\right]-\Delta t^2\cdot R\frac{\partial\bar{T}_0}{\partial\sigma}\nabla^2\hat{E}^{f,t+\Delta t},\end{aligned} \tag{21}$$

$$\nabla^2\chi^{t+\Delta t}=-\frac{\partial}{\partial\sigma}\dot{\sigma}^{t+\Delta t}+E^f-\hat{E}^{f,t+\Delta t}, \tag{22}$$

$$\nabla^2\psi^{t+\Delta t}=\nabla^2\psi^{t-\Delta t}+2\Delta t[E^A+L^{A,t+\Delta t}-f\nabla^2\chi^{t+\Delta t}], \tag{23}$$

where

$$\hat{E}^{l,t+\Delta t} = -\int_0^1 (\nabla^2 \chi^{t+\Delta t} - E^l) d\sigma .$$

If we use Eq. (17) to compute the velocity potential χ field, there will be problems related to small differences between large quantities. These include $\nabla^2\phi$, $R\bar{T}_0\nabla^2 \ln P_*$, and B_λ^T and B_φ^T in the E^B term. However, if Eqs. (21) and (22) are used, the computation of pressure gradient force terms involves small differences between small quantities. The aforementioned problems are therefore removed. This leads to stability in the numerical integration and is the key to the success of the present model for 30-day prediction experiments. Since the right-hand sides of Eqs. (21)—(23) contain $\dot{\sigma}$, χ, and ψ at time step $t+\Delta t$, which are to be solved numerically, the iteration method is required to find solutions for them. On the basis of numerical experimentation, five or less iterations are sufficient to converge the solutions with a high degree of accuracy.

All the basic parameters in the model may be expressed by means of spherical harmonics in the manner described by Zheng (1981). A spectral and pseudospectral method were used along the latitude and longitude, respectively. Using the scheme described previously, all nonlinear terms in the model may be computed efficiently and accurately. The initialization scheme of the nonlinear balance equations used in the present model is a new and efficient method recently proposed by Zheng (1987). The cloud formation scheme and radiative transfer calculations largely followed those presented by Liou and Zheng (1984) and Zheng and Liou (1986). In order to reduce the computational effort, the initial field of the Southern Hemisphere was computed from a symmetrical extension of that of the Northern Hemisphere. An even extension was used for all parameters, except the meridonal wind field.

III. MODEL VERIFICATION

In this section, we present a verification of the 30-day prediction for the 500 hPa geopotential height field, cloud cover, and radiation budget, as well as a discussion of the forecasting skill of the present model. The data used for initialization and verification are based on ECMWF objective analyses for the period from May 5 to June 3, 1982.

Figs. 1a and b show, respectively, the predicted and observed 500 hPa mean geopotential height fields in the Northern Hemisphere for the first 10-day period. A number of specific features are noted from the observed field. First, there are two arctic depressions located over the northern part of Kamchatka Peninsula and Greenland. The corresponding deep troughs, associated with cold air activities, are seen in the vicinity of Bajkal Lake in eastern Asia and over the eastern Atlantic coastal regions and Canada. Second, there is a broad trough over the western Pacific area. From the eastern Pacific to Atlantic Oceans, there are significant trough and ridge activities. In particular, ridges are shown in the eastern Pacific, over the midsection of the United States, and in central Atlantic regions. Troughs, on the other hand, preside over the western and eastern coastal areas of the United States. Finally, in the regions of eastern Asia and western Europe, the ridge in the north is coupled with a low in the south. The preceding circulation patterns are predicted well by the present model, which includes cloud formation and radiative heating rate calculations. Moreover, the subtropical highs in low latitudes are also predicted correctly by this model, including the subtropical highs south of the North American and Asian continents, and the northern Africa high.

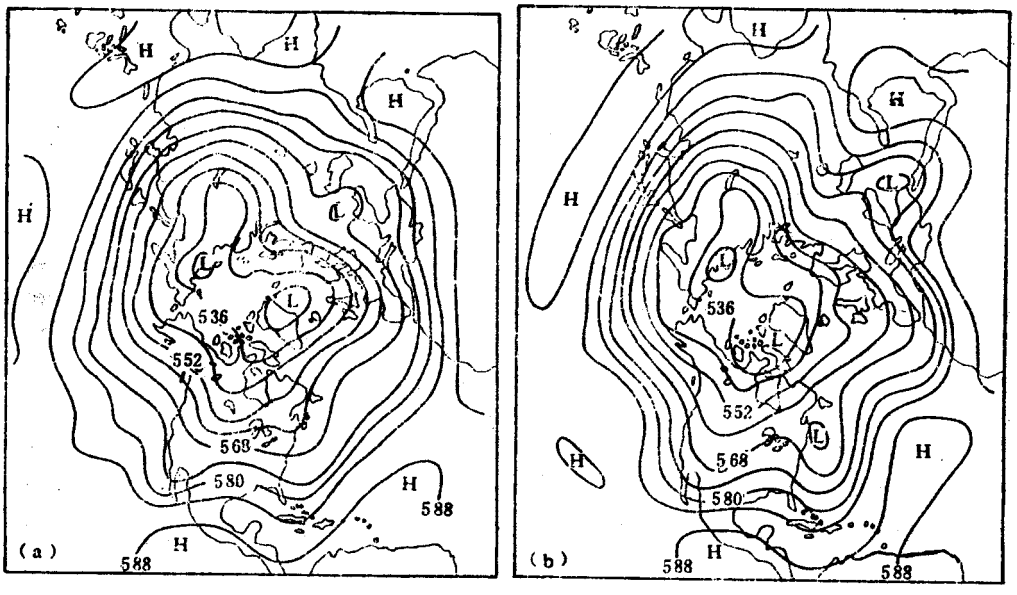

Fig. 1. (a) Predicted and (b) observed 500 hPa mean geopotential height fields in the Northern Hemisphere for the first 10-day period (May 5—May 14, 1982).

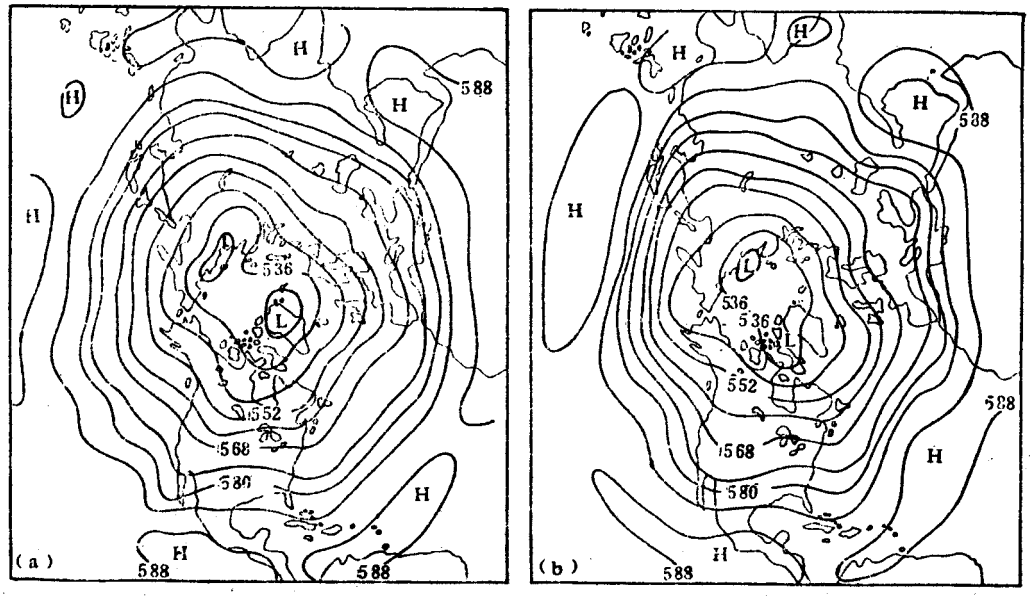

Fig. 2. (a) Predicted and (b) observed 500 hPa geopotential height fields for the 30-day period (May 5—June 3, 1982).

The predicted and observed 500 hPa mean geopotential fields for a 30-day period are shown in Fig.2a and b, respectively. In comparing these two 500 hPa fields, a close similarity is seen in the distribution of ridges and troughs, and the high and low centers, as well as their intensities. The 30-day prediction, in terms of the 500 hPa mean geopotential height field for the period covering May 5—June 3, 1982, appears to be quite accurate. The trough

located over the western part of the American continent, the ridge over the eastern region of the United States, and the trough along the eastern Atlantic coastal regions are correctly predicted. The predicted isopleths are in good agreement with observed values. The trough in the central Pacific, the zonal wind pattern in western Pacific regions, and the prevailing northwestern flow occurring over China and western Europe are also well-reproduced in the model.

During the period from May 5 to June 3, the numerous subtropical highs occurring over the Arabian Peninsula, Indian subcontinent, Indo-China, western Pacific, and in the vicinity of Mexico and Cuba are also correctly predicted in terms of their positions and intensities.

Next, we examine the predicted mean cloud cover for a 30-day period. The averaged cloud cover for the month of May (May 5—June 3) shown in Fig. 3 has the following specific features. There are well-defined ITCZs in the Atlantic and western Pacific, and over equatorial Africa and South America. Average cloud covers in some of these areas are as high as 80%. A large cloud cover, on the order of 80%, is also evident in the polar regions. There is significant cloudiness in midlatitudes that is associated with baroclinic storm activities. Low cloud covers on the order of 20% are mostly associated with the subtropical highs identified in Fig. 2b. In order to cross-check the 30-day mean cloud cover predicted from the model, a comparison was made with the July cloud climatology derived by Koenig et al. (1987). We recognize that the present 30-day average does not exactly coincide with the month of July. Nevertheless, this comparison offers a consistent check on the model performance for cloud cover prediction. The predicted cloud covers are in general agreement with July climatology values. Exceptions consist of larger cloud covers in the polar regions and lower cloud covers in some parts of the subtropical highs. It appears that the present model is adequate for forecasts of the total cloud cover.

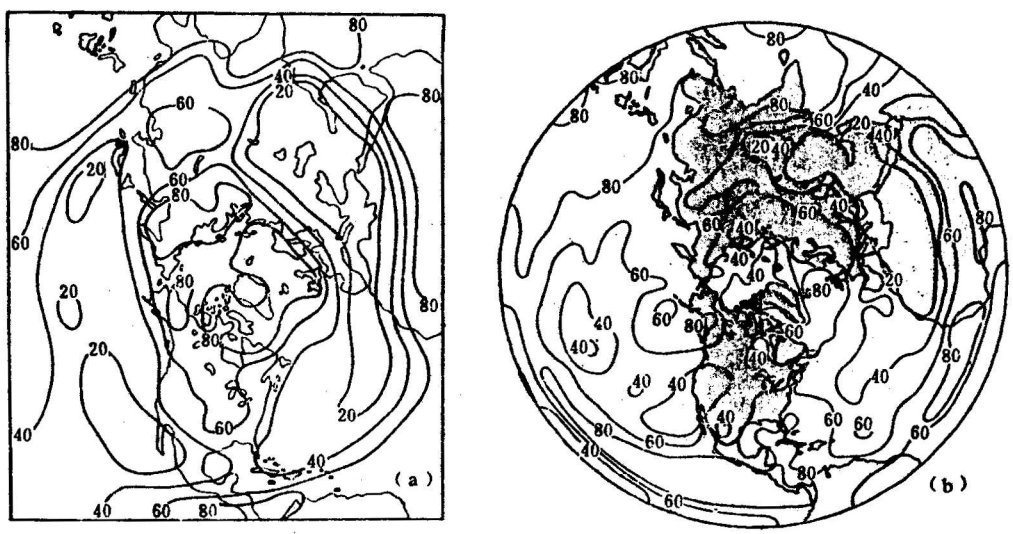

Fig. 3. (a) Predicted mean cloud covers averaged over the 30-day period and (b) July 3DNEPH total cloud covers (after Koenig et al., 1987).

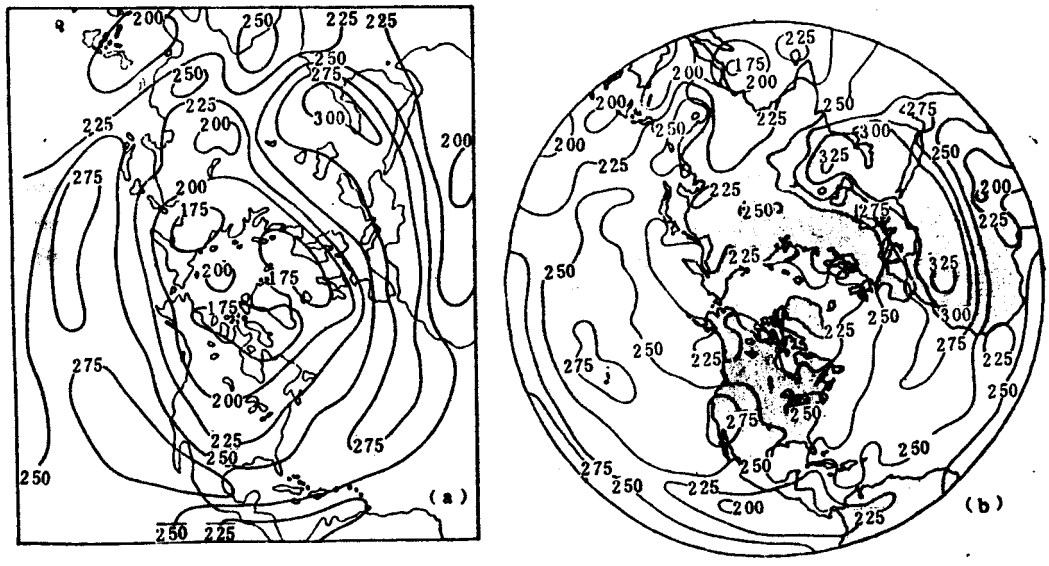

Fig. 4. (a) Predicted OLR fluxes averaged over the 30-day period and (b) OLR fluxes derived from NIMBUS 7 ERB data for July 1979 (after Koenig et al., 1987). Units are in W/m².

We also examine the averaged outgoing longwave radiation (OLR) fluxes predicted from the model for the 30-day period, shown in Fig. 4. The OLR patterns are basically controlled by the predicted cloud cover. In the ITCZ and polar regions, low OLR fluxes, with values on the order of 200 W/m², are shown. High OLR values are seen over the Afro-Asian deserts and subtropical highs. In particular, we note that small OLR fluxes over the Indian subcontinent and eastern Asia are associated with the monsoon. We compare the predicted OLR patterns with the July climatology values derived from ERB data (Koenig et al., 1987). In general, the mean OLR fluxes over the Northern Hemisphere, predicted by the model for the period May 5—June 3, are slightly smaller than the July values. This is due to a lower temperature in May than in July. However, the predicted OLR fluxes are correct in magnitude and agree with the predicted cloud field.

Finally, we present the forecast skill of the model in terms of RMS errors, E_{fo}, of the predicted 500 hPa geopotential height field (Fig. 5a) and 700 hPa temperature field (Fig. 5b) for a 30-day period. RMS errors, E_{po}, computed from persistence and denoted by dashed lines, are also shown for comparison purposes. In both cases, the E_{fo} do not increase significantly and they are all less than E_{po} for the 30-day period. The 30-day averaged RMS errors of the geopotential height fields from prediction and persistence, as well as the mean correlation coefficient for four pressure levels over the Northern Hemisphere, are listed in Table 1. The mean correlation coefficient, $\bar{r}$, representing the correlation coefficient between the observed and predicted geopotential height changes, is higher than 0.6 with an overall average of 0.645. The mean RMS errors of the predicted geopotential height field are less than those of persistence. An overall value of 79.9m is computed from the prediction, compared with a value of 102.7 m from persistence. We also inspect the forecast skill for the 30-day averaged 500 hPa geopotential height field for latitudes south of 30°N. The averaged $\bar{E}_{po}$ is 38.1 m, whereas $\bar{E}_{fo}$ is 35.8 m. In the 30-day period, E_{fo} remains

consistently smaller than E_{pe}, illustrating that the predicted results in the tropical region are satisfactory.

Table 1. Mean Correlation Coefficient, r, and RMS Errors for Forecast (E_{fo}) and Persistence (E_{pe}) for Geopotential Heights over the Northern Hemisphere

	200hPa	500hPa	700hPa	970hPa	Average
r	0.66	0.67	0.65	0.60	0.645
E_{fo} (m)	124.2	82.2	57.5	55.2	79.9
E_{pe} (m)	156.4	109.2	76.0	69.2	102.7

Note: The bar denotes a 30-day average.

IV. THE ROLE OF CLOUDS/RADIATION IN THE GENERAL CIRCULATION OF THE ATMOSPHERE

In this section, we investigate the effects of clouds and radiative heating on the general circulation of the atmosphere. This is done by inspecting the vertical velocity, and meridional and zonal winds predicted from the model.

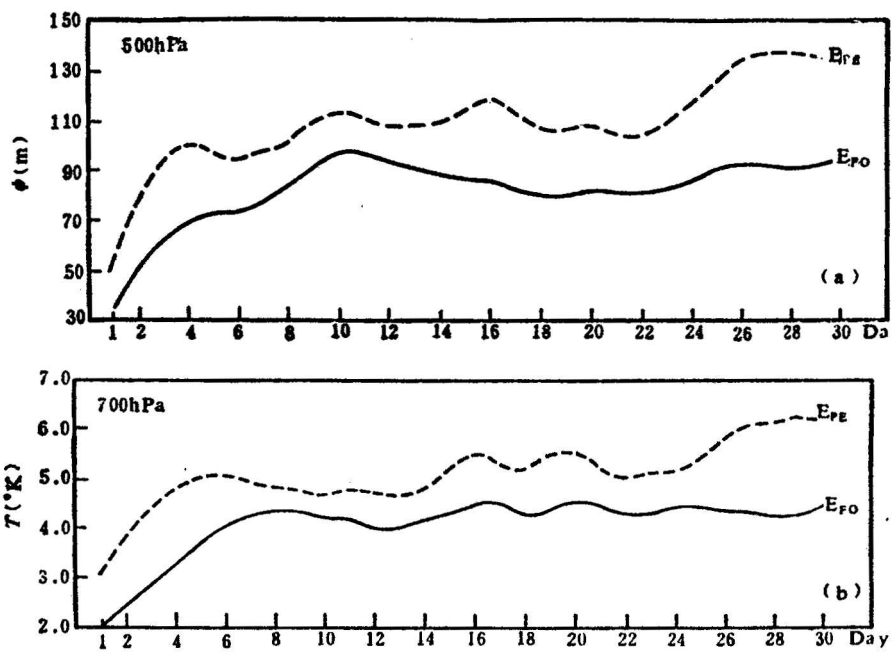

Fig. 5. The solid lines denote RMS errors, E_{fo}, of (a) the predicted 500 hPa geopotential height field and (b) 700 hPa temperature field, as functions of day. The dashed lines denote RMS errors, E_{pe}, computed from persistence.

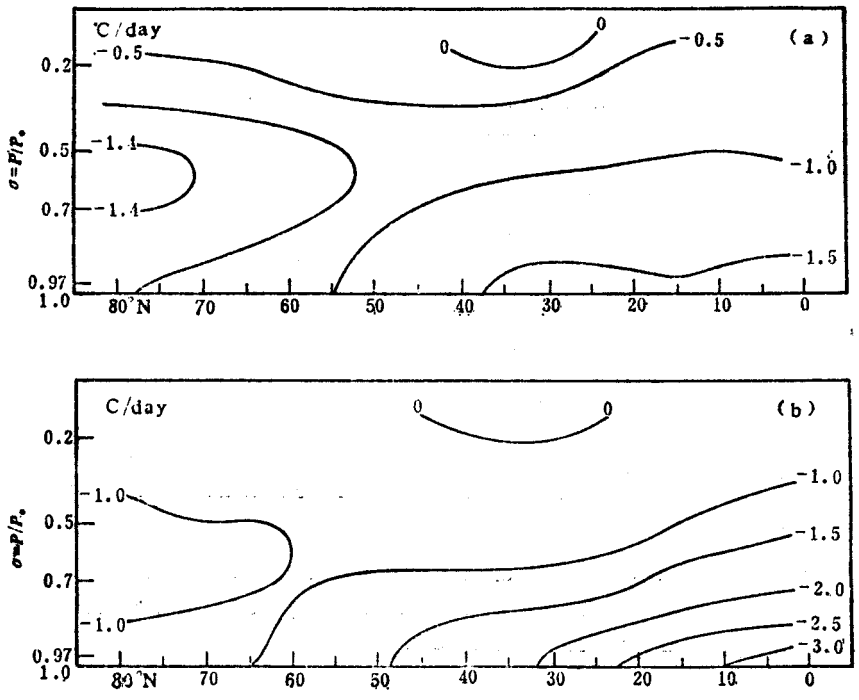

Fig. 6. (a) Averaged net radiative heating profile predicted from the model for the Northern Hemisphere covering May 5—June 3, and (b) same as (a) except without the cloud contribution, i.e., averaged radiative heating profile for a clear atmosphere.

1. *Radiative Heating Profiles*

We first present the mean zonally averaged, net radiative heating for the Northern Hemisphere predicted by the model for the period May 5—June 3. From Fig. 6a, it is clear that infrared cooling outweighs solar heating everywhere in the atmosphere. The largest cooling is found near the surface for latitudes south of about 40°N due to water vapor absorption and emission. In the polar region, a cooling maximum, produced by the prevalence of infrared cooling over solar heating, is also shown. In low and mid latitudes, radiative cooling generally decreases toward the upper troposphere. The top level of the present model is set at about 15 km. Thus cooling produced by carbon dioxide and ozone in the upper atmosphere is extremely small.

Fig. 6b shows the radiative cooling profile when clouds are removed from the model. This is the case corresponding to clear atmospheres. Without clouds, the cooling profile has a maximum near the surface in the tropics, which decreases with height, according to the vertical distribution of water vapor. A significant vertical gradient in cooling rates is shown in the tropical atmosphere. In midlatitudes, cooling rates are smaller than those occurring in the tropics. For this reason, a large horizontal gradient in cooling rates also exists between the tropics and midlatitudes.

In comparing the cooling rate patterns presented in Fig. 6a and b, we find that the clouds generated in the present model affect atmospheric radiative cooling in the following way. First, clouds suppress cooling in the lower troposphere, where cooling rates in the clear

atmosphere are reduced by about a factor of two. In polar regions, weaker solar heating leads to larger cooling in upper levels. As will be discussed below, radiative cooling profiles are directly associated with the vertical velocity. If the radiative cooling contribution is removed from the model, Q^R is equal to zero in the thermodynamic equation. This is the case referred to as "no radiation" in the model simulation.

The removal of clouds in the 30-day prediction experiments also has a direct impact on the latent heat release. Since the lower atmosphere has larger cooling rates without the presence of clouds, it is relatively stable. Thus the probability for the formation of cumulus convection would be significantly reduced in the prediction experiment. This, in turn, enhances the prevalence of atmospheric infrared cooling rates. The present cloud experiment in long-range numerical weather prediction differs from that in climatic perturbation studies. In the latter, the nonlinear effects between cloud/radiation interactions and cumulus convection are not considered and the clouds-climate experiment is simply referred to as the cloud radiative forcing experiment.

2. *Vertical Velocity*

In Figs. 7a, b and c we show the predicted mean vertical velocity profiles over a 30-day period. Fig. 7a illustrates the prediction results when clouds are formed in the model. In Fig. 7b, clouds are removed from the model so that the predicted vertical velocity corresponds to a clear atmosphere. Fig. 7c shows results without the incorporation of the atmospheric radiative heating term, Q^R, in the thermodynamic equations, i.e., radiative heating is zero everywhere in the atmosphere.

As is evident from Fig. 7a, there are three circulation patterns in the Northern Hemisphere. A strong upward motion is located at 500 hPa in the equatorial regions, with a maximum value of about 1×10^{-4} hPa/s. However, in the vicinity of 20° and 30°N, two downward motion maxima on the order of about 0.6×10^{-4} hPa/s are observed. These vertical velocity patterns constitute the Hadley circulation in the tropical region. In midlatitudes, two maxima of upward motion, with values of 0.7 and 0.4×10^{-4} hPa/s, are shown at 60° and 40°N, respectively. In high latitudes, however, there is a downward motion maximum. These vertical velocity distributions are associated with a distinct meridional circulation and another Hadley circulation.

When clouds are not accounted for in the model, significant changes in the circulation patterns take place in tropical regions. This is shown in Fig. 7b. Without the contribution of clouds in atmospheric radiative heating, strong downward motions are evident in equatorial regions. At the same time, upward motions are produced at about 30°N. The resulting circulation pattern is a reverse of the Hadley cell. In the middle part of high latitudes, the sign of the vertical motion remains the same, although its strength is somewhat reduced. The forcing of clouds through radiation and cumulus convection on atmospheric circulations may be understood from the cooling rate profiles presented in Figs. 6a and b. The presence of clouds in tropical regions reduces the vertical cooling rate gradient in the vertical and, at the same time, also decreases the horizontal cooling rate gradient between the tropics and midlatitudes. Without the contribution of clouds in the initial prediction experiment, the probability of cumulus convection is also substantially reduced during the experiments. This, in turn, enhances cooling near the surface and in the lower atmosphere. As pointed out in Liou and Zheng (1984), the vertical velocity is directly related to the Laplacian of radiative heating rates, $\nabla^2 Q^R$, and their vertical distribution, Q^R. Moreover, there are more

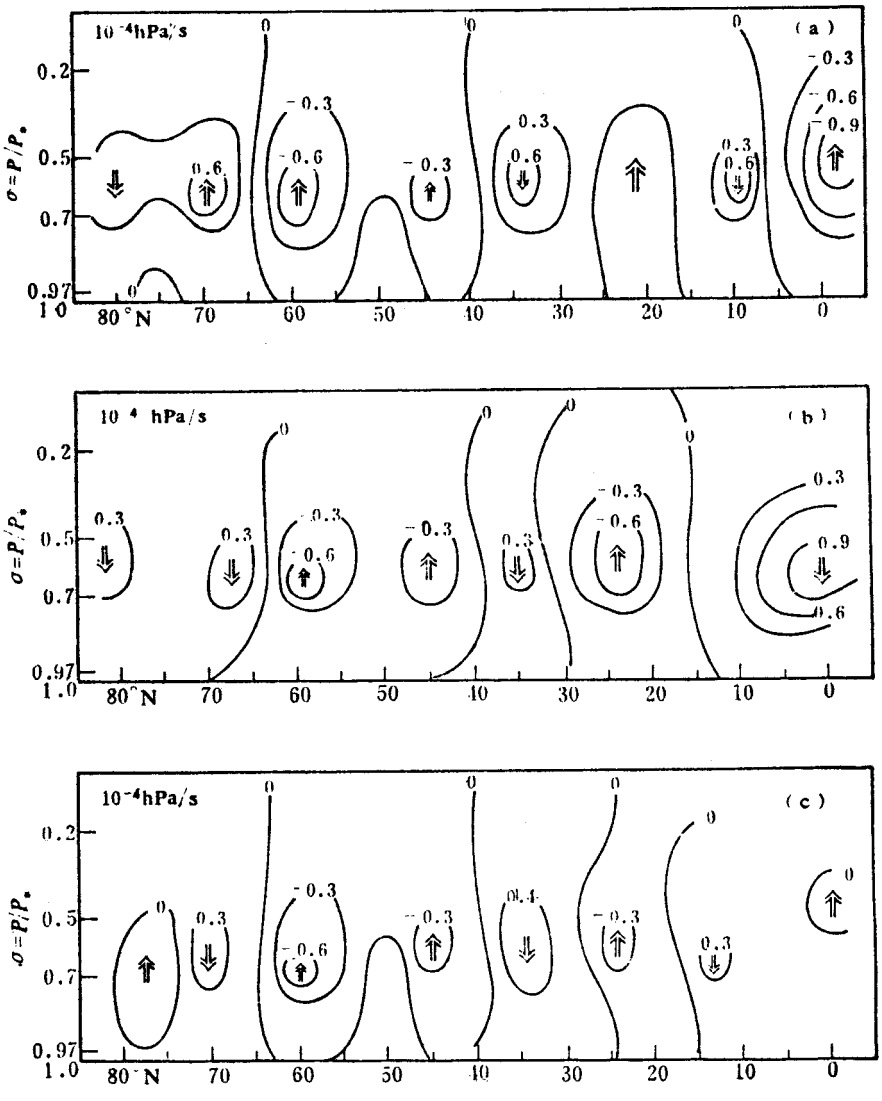

Fig. 7. (a) Predicted mean vertical velocity profiles over the 30-day period with interactive clouds and radiative heating calculations, (b) same as (a), except that clouds are removed from the model, and (c) same as (a), except that the radiative heating term, Q^R, is removed from the model.

types of land surfaces in the subtropical regions of the Northern Hemisphere than in the tropics. In the experiment, the sea surface temperatures were prescribed using the May climatological values, but the land surface temperatures were calculated from the surface energy budget equation. Without clouds, the subtropical land surfaces would be heated due to the direct transfer of solar fluxes. Subsequently, the land surface temperatures would be increased, as would be the transport of sensible heat (compared with that in the tropics). Without the modulation of clouds through radiative processes, there would be a meridional circulation in the tropics. Modifications in vertical velocity profiles are also apparent in mid-latitudes. However, at these latitudes, the circulation patterns are basically controlled by baroclinic processes. Thermal effects only contribute slightly to the development of the meridional circulation. In summary, cloud/radiation interactions and feedbacks are critically

important in the maintenance of the tropical Hadley circulation. Without an appropriate incorporation of cloud/radiation processes, it would not be possible to reproduce the general circulation in tropical and subtropical regions.

Fig. 7c shows the vertical velocity distribution when radiative heating, Q^R, is set to zero in the 30-day prediction. Without radiative cooling in the tropics, the vertical velocity in the middle troposphere is reduced by about 10^{-4} hPa/s. Thus the Hadley circulation would be significantly weakened. Slight reductions in upward and downward motions are also observed in other latitudes. Again, radiative heating contributions do not alter the basic structure of the meridional circulation. In our previous paper (Liou and Zheng, 1984), we pointed out the importance of radiative heating in the maintenance of the Hadley circulation in a simulation experiment for a 5-day prediction. The results of the present 30-day experiment are in line with our earlier findings. Moreover, the significant effects of cumulative radiative heating on the generation of strong upward motions in the tropics are noted.

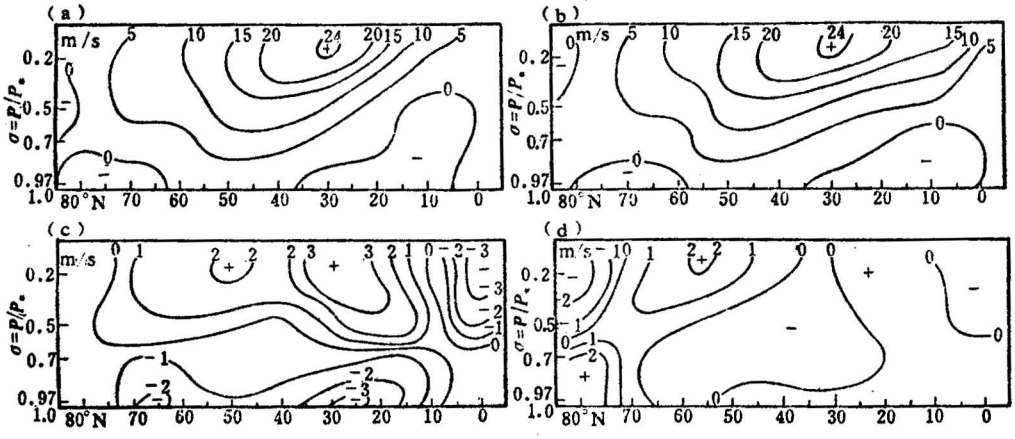

Fig. 8. (a) Observed mean zonal wind profile over the 30-day period (from May 5 to June 3), (b) predicted mean zonal wind profile over the 30-day period, (c) differences between the predicted mean zonal wind profiles with and without clouds, and (d) differences between the predicted mean zonal wind profiles with and without radiative heating calculations.

3. *Zonal Wind*

The observed zonal wind profile, averaged over the 30-day period from May 5 to June 3, is displayed in Fig. 8a. Prevailing westerlies dominate in the atmosphere with a jet located at about 200 hPa and 30°N. The intensity of this jet is about 25 m/s. From 10° to 90°N, except in the region from 40° to 70°N, weak easterly winds are evident in the lower atmosphere. Easterlies are also noted in the vicinity of about 500 hPa in polar regions. The predicted zonal wind profile is shown in Fig. 8b. The predicted westerlies and easterlies, in terms of their positions and magnitudes, are all in general agreement with observed values. In particular, the model correctly predicts the location and strength of the jet described previously.

Our next experiment investigates the effects of clouds on the maintenance of zonal winds. Clouds are not generated in the model in this experiment. We have subtracted the averaged zonal winds produced by this experiment from the results presented in Fig. 8b. The differences shown in Fig. 8c represent the contribution of cloud forcing to the zonal wind profile. The presence of clouds strengthens the westerlies in upper levels from about 20° to 80°N. Two maxima are noted at 30° and 50°N, with values of 3.4 and 2.0 m/s, respectively.

At the same time, the presence of clouds also enhances the easterlies in the lower atmosphere, close to the surface. The effects of clouds on zonal winds may be understood from the following two mechanisms. First, as pointed out in the discussion of the vertical velocity profile, the consideration of clouds in the model has the advantage of strengthening the Hadley circulation in low latitudes. In this case, the v component in low latitudes is northerly, whereas it is southerly in middle latitudes. Due to the Coriolis force, north of about 20°N, the poleward motion of the air mass in upper levels shifts to the west and consequently strengthens the westerlies. The air mass returns to equatorial regions, on the other hand, intensifying the easterlies. Second, when clouds are accounted for, the air mass is relatively warmer near the surface of equatorial regions, but colder in midlatitudes. This thermal structure results in the addition of westerlies and leads to a gradual establishment of the maximum located at about 30°N and 200 hPa. Due to thermal effects, the westerlies are reduced in the upper levels of equatorial regions.

The effects of radiative heating on the zonal wind profile are shown in Fig. 8d in terms of the differences in zonal winds. These differences are computed by subtracting the predicted zonal winds exclusive of the radiative heating contribution from the results presented in Fig. 8b. When atmospheric cooling rates are properly accounted for in the model, we would expect, in view of the cooling pattern displayed in Fig. 6a, that a relatively colder region would be established at latitudes between 80° and 85° N, and at 500—700 hPa. Thus levels south of this region would be relatively warmer. This thermal contrast leads to intensification of the westerlies in the Northern Hemisphere. We note that, when averaged over a 30-day period, the zonal wind increases by 2 m/s at about 60°N and 200 hPa. The influence of radiative heating on the zonal wind in other parts of the Northern Hemisphere appears to be quite small, however.

In summary, clouds and radiative heating both have a direct impact on the zonal wind profile. The zonal wind could be affected by 2—3 m/s per day in certain regions, if clouds and radiative heating profiles are not properly accounted for in prediction models.

V. CONCLUSIONS

In this paper, we have applied a seven-level global model to perform 30-day prediction experiments and investigated the effects of clouds and radiation on the general circulation of the atmosphere. In the model, specific attention was given to the spectral calculations of nonlinear terms in order to reduce the potential growth of small errors produced in the numerical integration. We devised an efficient method to overcome the problem involving small differences between large quantities occurring in the divergence equation, as well as in the pressure gradient force terms in the σ-coordinate in the vicinity of mountains. This allows the prediction experiments to be successfully carried out for a 30-day period. By using data from ECMWF objective analyses for the period from May 5 to June 3, 1982, the prediction skill of the model was demonstrated. We showed that the RMS of forecast errors is consistently less than that of persistence errors, and that the averaged correlation coefficient for all model levels is about 0.645. Further, we showed that the predicted results of the 30-day averaged 500 hPa geopotential height field compare closely with observed values. The predicted cloud and OLR fields are also consistent with July climatology data.

The model is then used to investigate the influence of clouds and radiative heating on predicted wind fields averaged over the period from May 5 to June 3. Highlights of the model results are summarized below.

(1) Clouds, through their coupling with the transfer of radiation, have a significant impact on the vertical velocity profile. In the tropics, the Hadley circulation is maintained by cloud/radiation interactions. If clouds are removed from the model, there is a strong cooling in the lower tropical regions, leading to the production of a reverse monthly mean circulation. Including the transfer of radiation in clouds leads to cooling at the cloud top and relative warming at the cloud base, and strengthens the upward motion in low latitudes.

(2) With the incorporation of clouds in the model, southerly winds of the mean monthly meridional circulation in the upper levels of low latitudes are in phase with the predicted vertical velocity and generate the correct Hadley circulation in the tropics. Moreover, the predicted mean monthly meridional circulation is in agreement with the observed data. Therefore, it appears that an improvement in the cloud prediction, which, in turn, would produce correct radiative heating distributions, could enhance the performance of long-range numerical weather prediction, especially in low latitudes.

(3) If clouds and radiative coupling are not properly accounted for in the model, the predicted monthly-averaged zonal winds deviate significantly from the observed values. The presence of clouds (compared with no clouds) strengthens westerlies in the middle and high levels in the model. There are two intensified centers located at about 25°—30°N and 50°—55°N, with mean monthly increases of about 3 and 2 m/s, respectively. These increases can contribute to the northward shift of the westerly jet stream frequently occurring in eastern Asia during the month of May.

REFERENCES

Gilchrist, A. (1977), An experiment in extended range prediction using a general circulation model and including the influence of sea-surface temperature anomalies, *Beitr. Phys. Atmos.*, **50**: 25—40.

Koenig, G., Liou, K.N. and Griffin, M. (1987), An investigation of cloud/radiation interactions using three-dimensional nephanalysis and earth radiation budget data bases, *J. Geophys. Res.*, **92**: 5540—5554.

Liou, K.N. (1986), Influence of cirrus clouds on weather and climate processes: A global perspective, *Mon. Wea. Rev.*, **114**: 1167—1199.

Liou, K.N., and Zheng, Q. (1984), A numerical experiment on the interactions of radiation, clouds, and dynamic processes in a general circulation model, *J. Atmos. Sci.*, **41**: 1513—1535.

Lorentz, E. (1984), Some aspects of atmospheric predictability, In *Problems and Prospects in Long and Medium Range Weather Forecasting*, D.M. Burridge and E. Kallen, Eds., Springer-Verlag, Berlin, 1—20.

Miyakoda, K., et al. (1983), Simulation of a blocking event in January 1977, *Mon. Wea. Rev.*, **111**: 846—869.

Miyakoda, K., Sirutis, J. and Ploshay J. (1986), One-month forecast experiments—without anomaly boundary forcings, *Mon. Wea. Rev.*, **114**: 2363—2401.

Ramanathan, V. (1987), The role of earth radiation budget studies in climate and general circulation research, *J. Geophys. Res.*, **92**: 4075—4095.

Shukla, J. (1981), Dynamic predictability of monthly means, *J. Atmos. Sci.*, **38**: 2547—2573.

Smagorinsky, J. (1969), Problems and promises of deterministic extended range forecating, *Bull. Amer. Meteor. Soc.*, **50**: 285—311.

Wetherald, R.T., and Manabe, S. (1988), Cloud feedback processes in a general circulation model, *J. Atmos. Sci.*, **45**: 1397—1415.

Zheng Qinglin (1979), A three-level filtered spectral model for the Northern Hemisphere, *Acta. Meteor. Sin.*, **37**: 36—43(in Chinese).

Zheng Qinglin (1981), A four-level primitive equation spectral model and its application to the numerical weather prediction, *Sci. Sin.*, **24**: 1121—1132.

Zheng Qinglin (1987), Experiments on the medium-range numerical weather prediction by using nonlinear balance equation initialization scheme in a seven-level spectral model, *J. Acad. Meteor.*, **2**: 337—346 (in Chinese).

Zheng, Q., and Liou K.N. (1986), Dynamic and thermodynamic influences of the Tibetan Plateau on the atmosphere in a general circulation model, *J. Atmos. Sci.*, **43**: 1340—1354.